International Journal Of
Industrial Electronics Control and Optimization
Print ISSN: 3517-2645
Online ISSN: 3568-2645
Homepage: https://ieco.usb.ac.ir/

Resource-Indexed Transfer Function Framework for Quantifying Frequency Interaction Authority in Hybrid IBR-Penetrated Power Systems

Shwan Sheikhahmadi | Ali Hesami Naghshbandy | Rahmatollah Mirzaei
Department of Electrical Engineering, University of Kurdistan, Sanandaj, Iran.[1]
Corresponding author's email: Hesami@uok.ac.ir

Article Info

Article type:
Research Article

Article history:
Received: **********
Received in revised form: **********
Accepted: **********
Published online: **********

Keywords:
Frequency stability,
Hybrid power systems,
Inverter-based resources,
Power system dynamics,
Resource interaction.

ABSTRACT

The rapid growth of inverter-based resources (IBRs) in modern power grids introduces dynamic characteristics that differ significantly from those of conventional synchronous generators, leading to notable changes in system response. Because generation technologies operate on different control timescales, traditional stability evaluation methods often cannot identify which resource type most affects frequency dynamics during disturbances. To address this gap, this paper proposes a resource-indexed H-matrix governance framework that quantifies pairwise interaction strength and directional asymmetries between resource categories via transfer-function analysis evaluated at the swing-mode eigenvalue and corroborated by a broadband frequency sweep. Two principal interaction pathways are characterized: an asymmetric synchronous-generator–grid-forming inertial coupling in which the SG retains primary dynamic dominance, and a negligible synchronization interaction between synchronous generators and grid-following inverters. We introduce a dimensionless governance ratio to translate interaction asymmetry into an illustrative operational classification scheme. Validation of the proposed framework is validated on the modified IEEE 9-bus test system, with a preliminary check on the IEEE 14-bus system, through modal participation factor analysis and nonlinear time-domain simulation, a broadband frequency-domain sweep, and an expanded Monte Carlo and one-at-a-time sensitivity analysis over ten controller parameters.

I. Introduction

The accelerated integration of inverter-based resources (IBRs) into power systems once dominated by synchronous generators is fundamentally changing system dynamics [1], [2]. Synchronous generators rely on their coupled rotating mechanical mass to regulate frequency inherently, whereas IBRs employ digital control algorithms whose operational principles differ markedly from those of electromechanical machines [3]. Consequently, the conventional analytical tools traditionally used to assess stability are proving progressively inadequate for describing mixed-technology systems [4], a limitation that introduces substantial complexity into operational planning as the energy transition gathers momentum [5].

Currently, IBRs typically operate in one of two control modes [6]. Grid-forming (GFM) inverters use control architectures such as virtual synchronous generator emulation or active power-frequency droop. These approaches allow GFM inverters to operate as voltage-source equivalents, providing synthetic inertia and enhancing system stability [7], [8]. The majority of installed IBR capacity, however, consists of grid-following (GFL) inverters that regulate their output current to track the prevailing grid voltage angle via a phase-locked loop (PLL), a feedback mechanism responsible for maintaining continuous synchronization with the network [9], [10]. GFL units lack rotational inertia and interact with the network differently [11].

When SGs, GFL, and GFM inverters operate simultaneously, their mutual interactions become increasingly complex and increasingly difficult to analyze as IBR penetration rises [12]. Recent analytical efforts have

Copyright © Author(s).
Publisher: University of Sistan and Baluchestan

examined GFM and GFL contributions in isolation [13], but none provide a quantitative characterization of asymmetric directional coupling. This gap is compounded by the partial overlap of the relevant timescales across a broad frequency spectrum, encompassing slow mechanical oscillations in the 0.5–2 Hz range, intermediate virtual-inertia emulation dynamics between 2 and 10 Hz, and fast electronic synchronization processes spanning 5–50 Hz. These overlapping phenomena challenge the conventional assumption that distinct physical processes occupy well-separated scales [14], [15].

Several established analytical methods are available to characterize hybrid system dynamics, but each exhibits particular deficiencies when applied to quantifying pairwise interaction strength among IBRs. Participation factor analysis [3], [16], [17], [18] distributes modal energy among state variables but cannot unambiguously identify the dominant resource when multiple machine types are operating simultaneously. Impedance-based methods [19], [20], [21], [22], [23], [24] effectively diagnose high-frequency instabilities at the point of coupling; however, their applicability is limited when characterizing system-wide governance. Aggregate inertia metrics [25], [26], [27], [28] estimate the global kinetic energy reserve but cannot account for network-mediated directional coupling asymmetries that ultimately determine frequency response authority. During transitional grid periods, system operators need resource-specific guidance on unit commitment; existing methods do not readily produce such interaction-aware operational directives.

We define governance as the asymmetric directional authority that one resource category exerts over another's frequency dynamics during electromechanical oscillations: specifically, the resource type, SG, GFM, or GFL, that establishes the dominant swing-mode response trajectory following a disturbance. Governance, in this sense, characterizes the competitive control interactions among co-located generation technologies, rather than simply aggregating installed capacity or individual performance contributions. It describes the directional, passive dynamic sensitivity of the linearized swing-mode response, not intentional control authority. Establishing this stronger causal link (e.g., via closed-loop transfer-function invertibility conditions or explicit constraints on control bandwidth) is a distinct problem identified for future work.

Matrix-based analytical frameworks have improved the spatial characterization of frequency dynamics. Green et al. [29] introduced a spatiotemporal inertia representation that captures power-to-frequency interactions using transfer function matrices. Wang et al. [30] extended this work by developing spatiotemporal damping metrics that distinguish self-damping from mutual-coupling effects. Both frameworks enhance understanding of distributed frequency phenomena, but they focus on bus-level quantities instead of resource-type interaction pathways. Their N×N dimensionality also makes practical operational interpretation more challenging.

PMU/WAMS-based spectral analysis (PSD/CSD) [31] identifies generator coherency groups without precise dynamic parameter knowledge, overcoming a key limitation of model-based methods such as ours (Section II-A). However, it detects general coupling rather than attributing directional dominance to specific source types, and it requires deployed PMU infrastructure that is unavailable during the planning stage, the focus of this framework. Thus, the two approaches are complementary: one for real-time monitoring of installed systems, and the other for evaluating proposed resource mixes during planning.

Building on the groundwork established in [29] and [30], this work introduces a machine-level governance framework that measures IBR interaction authority using frequency-domain analysis focused on the swing-mode frequency.

The H-matrix governance framework addresses the identified limitations by introducing specific innovations summarized in Table I.

TABLE I FRAMEWORK CAPABILITY COMPARISON

Capability	Part. Factors	Impedance	Sync. Coeff.	Agg. Inertia	Temp-Spatial	H-Matrix
Resource-type resolution	✗	✗	✗	✗	✗	✓
Directional coupling	Partial	✗	✗	✗	✗	✓
Topology sensitivity	✗	✓	Partial	✗	✓	✓
Operational scalability	✓	✗	✓	✓	✗	✓
Frequency dependence	✓	✓	✗	✗	Partial	✓

The principal contributions of this paper are as follows. First, a Resource-Indexed Interaction Framework is established, wherein a transfer function matrix indexed by resource category quantifies directional coupling asymmetry at the swing-mode frequency. Second, a Scalar Governance Metric is derived, which condenses interaction asymmetry into a single operational index and provides classification thresholds relevant to stability assessment.

The remainder of this paper is organized as follows. Section II develops the component-level state-space models and constructs the H-matrix. Section III validates the 2×2 formulation through two independent approaches. Section IV discusses practical implications and acknowledges limitations. Section V presents concluding observations.

II. SYSTEM MODELING AND H-MATRIX FRAMEWORK

A. Component-Level State-Space Models

1. Synchronous Generator Model

The synchronous generator is represented by a sixth-order model capturing mechanical swing dynamics, electromagnetic flux transients, automatic voltage regulation (AVR), and turbine-governor action [3]. The state vector is defined as $\mathbf{x}_{\mathrm{SG}} = [\delta, \omega, \acute{E}_q, \acute{E}_d, E_{fd}, P_m]^T$, where δ denotes rotor angle (rad), ω represents rotor speed deviation from synchronous speed (p.u.), $\acute{E}_q$ and $\acute{E}_d$ are quadrature and direct-axis transient internal voltages (p.u.), E_{fd} is field voltage (p.u.), and P_m denotes mechanical power (p.u.). The electromechanical swing dynamics are governed by:

$$\begin{aligned} \frac{\mathrm{d}\delta}{\mathrm{dt}} &= \omega_{base}\omega \\ 2\mathrm{H}\frac{\mathrm{d}\omega}{\mathrm{dt}} &= T_m - T_e - D(\omega - \omega_0) \end{aligned} \tag{1}$$

where H is the inertia constant (seconds), D is the mechanical damping coefficient (p.u.), $\omega_{base} = 2\pi f\ rad/s$ and $\omega_0 = 1$ p.u. Electrical power is computed via the Park transformation:$P_e = v_d i_d + v_q i_q$.

$$\begin{aligned} T_{d0}^{\prime}\frac{\mathrm{d}\acute{E}_q}{\mathrm{dt}} &= E_{fd} - \acute{E}_q - (X_d - X_d^{\prime})i_d \\ T_{q0}^{\prime}\frac{\mathrm{d}\acute{E}_d}{\mathrm{dt}} &= -\acute{E}_d + (X_q - X_q^{\prime})i_q \end{aligned} \tag{2}$$

where $T_{d0}^{\prime}$ *and* $T_{q0}^{\prime}$ are open-circuit transient time constants (seconds), X_d and X_q denote synchronous reactances (p.u.), and $X_d^{\prime}$ and $X_q^{\prime}$ represent transient reactances (p.u.).

$$\begin{aligned} T_a\frac{\mathrm{d}E_{fd}}{\mathrm{dt}} &= K_a(V_{ref} - V_{t)} - E_{fd} \\ T_{gov}\frac{\mathrm{d}P_m}{\mathrm{dt}} &= P_{ref} - P_m - \frac{1}{R_{gov}}\omega \end{aligned} \tag{3}$$

where T_{gov} is the governor time constant (seconds), P_{ref} is the mechanical power reference (p.u.), and R_{gov} denotes the droop coefficient (p.u.). Linearization around the operating point $(P_0, Q_0, V_0, \theta_0)$ obtained from load flow yields the state-space representation [32]:

$$\begin{aligned} \dot{\mathbf{x}}_{\mathrm{SG}} &= \mathbf{A}_{\mathrm{SG}}\mathbf{x}_{\mathrm{SG}} + \mathbf{B}_{SG}\mathbf{u}_{SG} \\ \mathbf{y}_{\mathrm{SG}} &= \mathbf{C}_{\mathrm{SG}}\mathbf{x}_{\mathrm{SG}} + \mathbf{D}_{SG}\mathbf{u}_{SG} \end{aligned} \tag{4}$$

where $\mathbf{A}_{\mathrm{SG}} \in \mathbb{R}^{6\times6}$, $\mathbf{B}_{SG} \in \mathbb{R}^{6\times2}$,$\mathbf{C}_{\mathrm{SG}} \in \mathbb{R}^{2\times6}$, and $\mathbf{D}_{SG} \in \mathbb{R}^{2\times2}$. The input vector $\mathbf{u}_{\mathrm{SG}} = [v_d, v_q]$ comprises terminal voltage components, while the output vector $\mathbf{y}_{\mathrm{SG}} = [i_d, i_q]^T$ contains injected current components.

2. Grid-Following Inverter Model

The GFL inverter implements a cascaded control architecture comprising PLL synchronization, outer power control loops, inner current control loops, and an LCL filter interfacing with the network [6], [9]. The state vector

$$\begin{aligned} \mathbf{x}_{\mathrm{GFL}} = [&\theta_{PLL}, \omega_{PLL}, P_m, Q_m, \xi_P, \xi_Q, \gamma_d, \gamma_q, \\ &v_d^*, v_q^*, i_{\ell d}, i_{\ell q}, v_{cd}, v_{cq}, i_{gd}, i_{gq}]^T \end{aligned}$$

encompasses 16 states representing angle tracking, frequency estimation, power measurement, power control integrators, current references, modulation voltages, filter inductor currents, capacitor voltages, and grid-side currents. The synchronous reference frame PLL employs a proportional-integral (PI) structure to track grid voltage angle and estimate frequency deviation [10]:

$$\begin{aligned} \frac{\mathrm{d}\theta_{PLL}}{\mathrm{dt}} &= \omega_0 + \omega_{PLL} + K_{p,PLL}v_{cq} \\ \frac{\mathrm{d}\omega_{PLL}}{\mathrm{dt}} &= K_{i,PLL}v_{cq} \end{aligned} \tag{5}$$

where θ_{PLL} is the estimated grid angle (rad), ω_{PLL} represents frequency deviation (p.u.), v_{cq} denotes quadrature-axis capacitor voltage in the PLL reference frame (p.u.), and $K_{p,PLL}$ and $K_{i,PLL}$ are PLL controller gains. Active and reactive powers are measured through low-pass filters with bandwidth ω_c (rad/s) [33]:

$$\begin{aligned} \frac{\mathrm{d}P_m}{\mathrm{dt}} &= -\omega_c P_m + \omega_c(\frac{3}{2})(v_d i_{\ell d} + v_q i_{\ell q}) \\ \frac{\mathrm{d}Q_m}{\mathrm{dt}} &= -\omega_c Q_m + \omega_c(\frac{3}{2})(v_q i_{\ell d} - v_d i_{\ell d}) \end{aligned} \tag{6}$$

where (v_d, v_q) and $(i_{\ell d}, i_{\ell q})$ represent voltage and current at the filter capacitor in the local dq frame.

Outer power control loops employ PI regulators to generate current references:

$$\begin{aligned} \frac{\mathrm{d}\xi_P}{\mathrm{dt}} &= P_{ref} - P_m \\ i_d{}^* &= K_{p,pq}\big(P_{ref} - P_m\big) + K_{i,pq}\xi_P \\ \frac{\mathrm{d}\xi_Q}{\mathrm{dt}} &= Q_{ref} - Q_m \\ i_q{}^* &= -K_{p,pq}\big(Q_{ref} - Q_m\big) - K_{i,pq}\xi_Q \end{aligned} \tag{7}$$

where $K_{p,pq}$ and $K_{i,pq}$ denote power control gains, and $(i_d{}^*, i_q{}^*)$ represent desired current references. Inner current control loops regulate filter inductor currents through PI controllers:

$$\begin{aligned} \frac{\mathrm{d}\gamma_d}{\mathrm{dt}} &= i_d{}^* - i_{\ell d} \\ v_d{}^* &= K_{p,cc}v_{cq}(i_d{}^* - i_{\ell d})K_{i,cc}\gamma_d \end{aligned} \tag{8}$$

with similar expressions for the quadrature axis, where $K_{p,cc}$ and $K_{i,cc}$ are current controller gains, and $(v_d{}^*, v_q{}^*)$ represent modulation voltage commands. Computational delay inherent in digital control implementation is approximated through first-order lag dynamics with time constant $\tau \approx 1.5/f_{sw}$, where $f_{sw} = 10$ kHz is the switching frequency [34].

The LCL filter dynamics in the rotating dq-frame are:

$$\begin{aligned} L_f\frac{\mathrm{d}i_{\ell d}}{\mathrm{dt}} &= v_d{}^* - R_f i_{\ell d} - v_{cd} + \omega_0 L_f i_{\ell q} \\ L_f\frac{\mathrm{d}i_{\ell q}}{\mathrm{dt}} &= v_q{}^* - R_f i_{\ell q} - v_{cq} - \omega_0 L_f i_{\ell d} \\ C_f\frac{\mathrm{d}v_{cd}}{\mathrm{dt}} &= i_{\ell d} - i_{gd} + \omega_0 C_f v_{cq} \\ C_f\frac{\mathrm{d}v_{cq}}{\mathrm{dt}} &= i_{\ell q} - i_{gq} - \omega_0 C_f v_{cd} \\ L_g\frac{\mathrm{d}i_{gd}}{\mathrm{dt}} &= v_{cd} - v_{td} - R_g i_{gd} + \omega_0 L_g i_{gq} \end{aligned} \tag{9}$$

$$L_g \frac{\mathrm{d}i_{gq}}{\mathrm{dt}} = v_{cq} - v_{tq} - R_g i_{gq} - \omega_0 L_g i_{gd}$$

where L_f and R_f are filter-side inductance and resistance, C_f is the filter capacitance, L_g and R_g denote grid-side inductance and resistance, and (v_{td}, v_{tq}) represent terminal voltage at the point of common coupling. The configuration of the GFL IBR is depicted in Fig. 1.

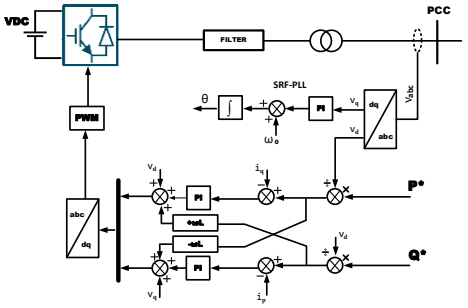


Fig. 1. GFL Inverter and the control structures in synchronous dq frame.

3. Grid-Forming Inverter Model

The GFM inverter emulates virtual synchronous machine (VSM) characteristics [7], [35], [36]. The 18-state vector

$$\mathbf{x}_{\mathrm{GFM}} = [\theta, \omega, V_{ref}, P_m, Q_m, v_d^*, v_q^*, \gamma_{id}, \gamma_{iq}, i_{\ell d}, i_{\ell q}, v_{cd}, v_{cq}, i_{gd}, i_{gq}, v_{td}, v_{tq}, V_{meas}]^T$$

comprises virtual rotor states, voltage control, power measurement, current control, and LCL filter dynamics. The virtual synchronous machine dynamics implementing synthetic inertia are:

$$\begin{aligned} \frac{\mathrm{d}\theta}{\mathrm{dt}} &= \omega_{base}\omega \\ 2\mathrm{H}_{virt}\frac{\mathrm{d}\omega}{\mathrm{dt}} &= P_{ref} - P_m - D_{virt}\omega \\ &\quad - D_P\omega_{base}\omega \end{aligned} \tag{10}$$

where θ is the virtual rotor angle (rad), ω denotes frequency deviation (p.u.), H_{virt} represents the virtual inertia constant (seconds), D_{virt} is the virtual damping coefficient (p.u.), and D_P implements active power droop (p.u.). Eq. (10b) directly parallels the SG swing Eq. (1b), with virtual parameters replacing physical quantities. The droop term $D_P\omega_{base}\omega$ provides proportional frequency support analogous to governor droop in synchronous machines.

Reactive power droop regulates voltage magnitude according to:

$$\frac{\mathrm{d}V_{ref}}{\mathrm{dt}} = -\omega_v\left(V_{ref} - \mathrm{V}^*\right) - \omega_v D_q Q_m \tag{11}$$

where ω_v is the voltage control bandwidth (rad/s), V^* denotes the voltage setpoint (p.u.), and D_q represents reactive droop coefficient (p.u.). Active and reactive power measurements employ an identical filtering structure to GFL (Eq. (7)). Voltage references in the *dq*-frame are generated as:

$$\begin{aligned} v_d{}^* &= -\omega_v v_{cd} + \omega_v V_{ref} \\ v_q{}^* &= -\omega_v v_{cq} \end{aligned} \tag{12}$$

providing voltage magnitude control (through *d*-axis) while maintaining zero steady-state reactive voltage (*q*-axis regulation). Current control and LCL filter dynamics follow structures analogous to Eq. (9), with parameters matched to ensure consistent hardware representation across inverter types. The configurations of GFM IBR are depicted in Fig. 2.

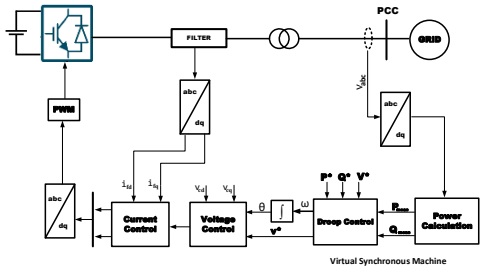


Fig. 2. GFM Inverter and the control structures in synchronous dq frame.

B. Resource-Indexed Interaction Transfer Function Matrix

The H-matrix quantifies the strength of interaction between distinct resource categories by applying frequency-domain transfer-function analysis at the swing-mode eigenvalue. This formulation permits unambiguous assessment of the pairwise IBR interaction pathways that bear upon frequency-control authority. In contrast to bus-indexed admittance matrices or nodal impedance matrices, the H-matrix adopts resource-type indexing that directly juxtaposes control mechanisms spanning diverse generation technologies.

Consider a power network containing n heterogeneous generation units (SGs, GFMs, GFLs, etc.), each contributing dynamic states encoding electromechanical dynamics, control loops, and network interfaces. The unified small-signal model takes the form:

$$\begin{aligned} \dot{\mathbf{x}} &= \mathbf{A}_{\mathrm{cl}}\mathbf{x} + \mathbf{B}_{\mathrm{h}}\Delta\mathbf{P}_{\mathrm{inj}} \\ \Delta\dot{\boldsymbol{\omega}} &= \mathbf{C}_{\mathrm{h}}\mathbf{x} \end{aligned} \tag{13}$$

where $\mathbf{x} \in \mathbb{R}^{\boldsymbol{m}}$ contains all system states (m depends on model fidelity), $\mathbf{A}_{\mathrm{cl}} \in \mathbb{R}^{m\times m}$ is the closed-loop state matrix including network coupling, $\mathbf{B}_{\mathrm{h}} \in \mathbb{R}^{m\times n}$ routes power disturbances to appropriate states, $\Delta\mathbf{P}_{\mathrm{inj}} = [\Delta\mathbf{P}_1, \Delta\mathbf{P}_2, \ldots, \Delta\mathbf{P}_{\mathrm{n}}]^T$, and $\mathbf{C}_{\mathrm{h}} \in \mathbb{R}^{n\times m}$ extracts frequency deviations, $\Delta\boldsymbol{\omega} = [\boldsymbol{\omega}_1, \boldsymbol{\omega}_2, \ldots, \boldsymbol{\omega}_{\mathrm{n}}]^T$.

The frequency-domain transfer function relating power disturbances to frequency responses is:

$$\mathbf{H}(\mathrm{s}) = \mathbf{C}_h(\mathrm{s}\mathbf{I} - \mathbf{A})^{-1}\mathbf{B}_h \tag{14}$$

Element $\mathrm{H}_{ij}(\mathrm{s})$ quantifies how resource *i*'s frequency $\Delta\boldsymbol{\omega}_{\boldsymbol{i}}$ responds to resource *j*'s power disturbance $\Delta\mathbf{P}_{\mathrm{j}}$. This is a directional transfer function: generally $\mathrm{H}_{ij}(\mathrm{s}) \neq \mathrm{H}_{ji}(\mathrm{s})$, capturing asymmetric coupling.

Among all eigenvalues of $\mathbf{A}_{\mathrm{cl}}$, the swing mode $s_{swing} = \sigma_{swing} + j\omega_{swing}$ is identified through a three-criterion screening process applied to all eigenvalues $\lambda_k = \sigma_k + j\omega_k$. Frequency range: $0.5 < f_k < 2.5$ Hz, where $f_k = |\omega_k|/(2\pi)$. Electromechanical participation: $\sum_{i\in\{\delta,\omega\}}|v_{ki}|^2/\sum_j|v_{kj}|^2 > 0.5$, where v_{ki} are right eigenvector elements. Minimum damping: $\zeta_k > 0.01$, where $\zeta_k = -\sigma_k/|\lambda_k|$.

Unlike DC or high frequencies, the swing mode captures the frequency range where inertial energy storage/release dominates, electromagnetic coupling through network admittance is strongest, damping from controls and physical mechanisms interacts, and synchronization stability is determined. Evaluating $\mathrm{H}(s_{swing})$ isolates the interaction strength at the critical frequency at which governance-authority manifests during transient disturbances.

At $s = s_{swing}$, the transfer function matrix yields complex-valued elements:

$$\mathbf{H}(s_{swing}) = \begin{pmatrix} H_{11}(s) & \dots & H_{1n}(s) \\ \vdots & \ddots & \vdots \\ H_{n1}(s) & \dots & H_{nn}(s) \end{pmatrix} \quad (15)$$

C. Governance Ratio Derivation and Physical Interpretation

The absolute magnitudes of Eq. (15) exhibit strong dependence on component parameters (H, H_{virt}, D), making direct comparison across operating points challenging. Normalization by self-response isolates coupling effects from parameter scaling [37]:

$$\Lambda_{ij} = \frac{|H_{ij}(s_{\mathrm{swing}})|}{|H_{jj}(s_{\mathrm{swing}})|} \quad \text{for} \quad i \neq j \quad (16)$$

The dimensionless ratio Λ_{ij} quantifies how strongly resource *i*'s frequency responds to a disturbance at resource *j* relative to how resource *j* responds to its own disturbance. A value $\Lambda_{ij} > 1$ indicates that unit *i* is more sensitive to unit *j*'s power than unit *j* is to itself.

The governance ratio between any resource pair (*i*, *j*) quantifies bidirectional asymmetry:

$$\Gamma_{ij} = \frac{\Lambda_{ij}}{\Lambda_{ji}} = \frac{|H_{ij}|/|H_{jj}|}{|H_{ji}|/|H_{ii}|} \quad (17)$$

Two regimes follow directly from this definition. When $\Gamma_{ij} \gg 1$ (Dominance of Resource *i*), resource *i* dictates the frequency reference and resource *j* is forced to follow, showing higher perturbations. When $\Gamma_{ij} \ll 1$ (Dominance of Resource *j*), the relationship reverses, and resource j governs resource i. Physical basis of the metric: Λ_{ij} measures how strongly resource *i*'s frequency state responds, per unit of its own self-response, to a disturbance originating at resource *j*, the frequency-domain analogue of relative kinetic/torque sensitivity between coupled rotating and virtual-rotating masses. Because Λ_{ij} and Λ_{ji} are each normalized by a different resource's self-response, their ratio Γ_{ij} isolates the asymmetry in this sensitivity indicating which resource is comparatively immune to the other's disturbances and which is comparatively reactive (see Section I for the distinction between this passive dynamic dominance and intentional control authority).

Note that $\Gamma_{ji} = 1/\Gamma_{ij}$ by construction, so each unordered resource pair (i, j) is characterized by a single governance value. For n-resource systems, this produces n(n-1)/2 unique governance ratios characterizing all pairwise interactions.

D. Broadband Frequency-Domain Analysis

The governance classifications reported in this paper are computed from H(s) evaluated at the swing-mode eigenvalue only (Eq. 16). To assess how representative this single-point evaluation is of the underlying dynamics, we swept $|H_{ij}(j\omega)|$ over 0.1-20 Hz at the baseline operating point (60% penetration, *SCR* = 2).

As shown in Fig. 3, three of the four 2×2 H-matrix elements (H_{11}, H_{12}, H_{21}) attain local maxima within the electromechanical band within 1% of the identified swing-mode frequency (1.616 Hz): peaks occur at 1.626 Hz, 1.604 Hz, and 1.604 Hz, respectively. H_{22} (the GFM self-response term) exhibits a distinct local peak at 1.368 Hz (-15.4% relative to the swing mode) with a visible notch near the swing frequency itself, indicating that the GFM's self-response is shaped by an additional internal resonance not fully coincident with the network-coupled electromechanical mode; we note this as a limitation of single-frequency evaluation for diagonal terms specifically (Section V-C).

This broadband analysis further supports the GFL-negligibility assumption underlying the 2×2 reduction (Section IV): when we evaluate the general n-resource formulation of Eq. (16) for the three-resource case (SG, GFL, GFM), the coupling from GFL into the SG-GFM subsystem remains approximately 2.8 orders of magnitude smaller than direct SG-GFM coupling at the swing frequency

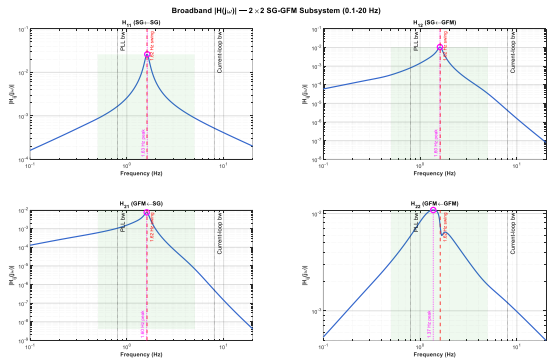


Fig. 3. Broadband magnitude response $|H_{ij}(j\omega)|$ of the 2×2 SG-GFM subsystem over 0.1–20 Hz.

($H_{SG,GFL}$ = 1.01×10⁻⁵, $H_{GFM,GFL}$ = 1.75×10⁻⁵, versus $H_{SG,GFM}$ = 1.04×10⁻²). The converse coupling from SG or GFM into GFL is substantial, as expected for a GFL that tracks system frequency through its PLL; this asymmetry is consistent

with, rather than contrary to, the reduction, since it is specifically the influence on the SG-GFM subsystem that must be small to justify truncating the GFL state. We do not claim this single-point evaluation captures interaction behavior at sub-synchronous or PLL-control-mode frequencies (5–50 Hz); extending the framework to a frequency-dependent formulation is identified as future work.

III. Case study

A. Hybrid System Architecture and Operating Conditions

The modified IEEE 9-bus test system in Fig. 4 includes one SG, one GFL inverter, and one GFM inverter. Developed in MATLAB, it models a transition regime in which neither conventional machines nor IBRs dominate the generation mix, preserving the fundamental dynamics of mixed synchronous-generator/inverter-based-resource (SG-IBR) systems while allowing comprehensive parametric analysis.

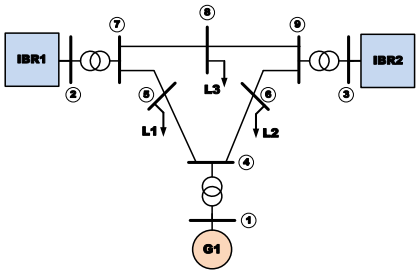


Fig. 4. Modified IEEE 9-bus hybrid system topology.

Network strength is measured by the short-circuit ratio (SCR), defined at the point of common coupling as the available fault current normalized by the rated inverter current [38]. To assess stability under varying grid conditions, we scale the base network impedances as follows:

$$\mathrm{Z}_{line}(SCR) = \mathrm{Z}_{base}\frac{SCR_{base}}{SCR} \tag{18}$$

where $SCR_{base} = 3.4$ represents the unmodified configuration and SCR in [1.5,5], spans weak, intermediate, and strong grid regimes. This impedance scaling preserves power flow convergence characteristics while systematically varying the electrical coupling strength between generators and loads. IBR penetration level is expressed as the fraction of total installed capacity supplied by inverter-based resources:

$$Penetration = \frac{P_{GFM} + P_{GFL}}{P_{SG} + P_{GFM} + P_{GFL}} \tag{19}$$

The nominal operating point is established at 60% IBR penetration and SCR = 2, representing balanced SG-IBR dispatch. Penetration is subsequently varied from 10% to 90% in 5% increments by proportionally adjusting SG and IBR output powers while holding total generation constant to satisfy load demand. Combined with variation across eight discrete SCR values, this parametric sweep generates 136 distinct operating points (17 × 8), enabling statistically robust analysis of governance characteristics over the entire operational envelope.

Power disturbances are injected into electromechanical state equations through the input matrix $\mathbf{B}_h \in \mathbb{R}^{40\times2}$, defined by examining mechanical power terms in swing equations. Frequency responses are extracted through the output matrix $\mathbf{C}_h \in \mathbb{R}^{2\times40}$, selecting rotor speed states from the full state vector. The frequency-domain transfer function relating power disturbances to frequency responses is then evaluated according to Eq. (14). The matrix $\mathbf{H}(\mathrm{s}) \in \mathbb{C}^{2\times2}$ contains four transfer functions:

$$\mathbf{H}(\mathrm{s}) = \begin{pmatrix} H_{11}(s) & H_{12}(s) \\ H_{21}(s) & H_{22}(s) \end{pmatrix} \tag{20}$$

The diagonal elements (H_{11}, H_{22}) represent self-response, while off-diagonal (H_{12}, H_{21}) elements capture cross-coupling and quantify the strength and directionality of resource-to-resource interaction: H_{12} measures SG frequency response to GFM power disturbances (SG-to-GFM interaction), while H_{21} captures GFM response to SG disturbances (GFM-to-SG interaction). The 2×2 model focuses on the main SG to GFM interaction pathway, while the GFL contribution, which is not included, is addressed in Section IV.

The swing-mode eigenvalue s_{swing} is selected as the mode satisfying all criteria with the minimum damping ratio, as this mode determines transient response characteristics and stability margins. For the baseline operating point, the swing mode is identified as $s_{swing} = -0.527 + j10.153\ rad/s$, corresponding to $f_{swing} = 1.616$ Hz with damping $\zeta_{swing} = 5.18\%$.

To clarify the physical meaning of governance ratio Γ, consider the baseline operating point (60% IBR penetration, SCR = 2): the H-matrix yields $|H_{11}| = 0.02615$, $|H_{12}| = 0.01057$, $|H_{21}| = 0.00739$, $|H_{22}| = 0.00732$, giving Γ= 5.11 (Fig. 5). The normalized dominance ratios, $\Lambda_{12} = 1.4434$ and $\Lambda_{21} = 0.2825$, show the strength of interactions in each direction. The governance ratio can also be seen as an interaction asymmetry index.

The governance thresholds presented in Table II were empirically validated through statistical analysis of 136 operating points. Kruskal-Wallis tests [39] confirm the three regimes represent statistically distinct dynamic populations in swing-mode damping with all pairwise comparisons significant under Bonferroni correction (α = 0.0167).

TABLE II Thresholds guidance

Regime	Threshold	Characteristics
SG-Dominant	Γ ≥ 4	SG retains synchronizing authority over the swing mode, while GFM acts as a controlled follower.
Transition	1.5 ≤ Γ < 4	Neither resource dominates.
GFM-Dominant	Γ < 1.5	GFM increasingly sets the swing-mode trajectory.

These threshold values are derived from, and specific to, the parametric sweep of the modified 9-bus system studied here; they should be interpreted as an illustrative classification scheme rather than universally applicable boundaries. Γ=4 and Γ=1.5 were selected as round, interpretable values approximating the regime separation observed via Kruskal-Wallis testing within this study's 136-point sweep; they have not been optimized via ROC analysis, cross-validation, or validated on an independent dataset. A rigorous derivation of thresholds validated across multiple network topologies, controller parameterizations, and system sizes is beyond the present study's scope and is identified as an important direction for future work.

At the 60% penetration / SCR = 2 baseline, Γ = 5.11 places the system in the SG-Dominant regime, confirming that the SG retains synchronizing authority (91.2% participation) while the GFM contributes supplementary damping (8.8%) without displacing the SG as the primary frequency reference.

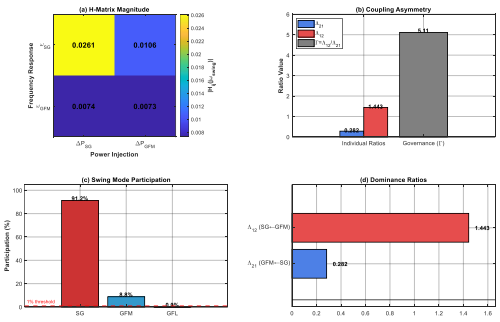


Fig. 5. H-matrix (baseline operating point). (a) Element magnitudes. (b) Asymmetric coupling & Governance ratio. (c) Swing Mode Participation. (d) Dominance ratios.

The integration of these validated thresholds into the overall assessment method is summarized by the flowchart in Fig. 6.

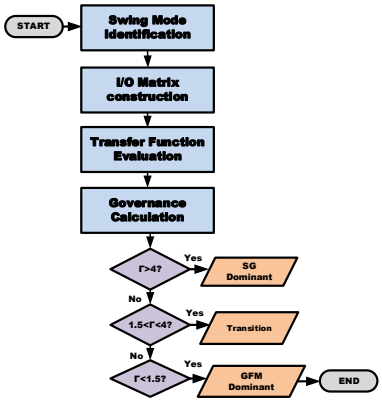


Fig. 6. Flowchart of the proposed method.

As shown in Fig. 7, Γ decreases from 13.94 at 10% IBR penetration to a minimum of 4.74 at 80%, a net 65% reduction in the governance ratio. The system remains within the SG-Dominant regime (Γ≥4) across the entire 10–90% range and never crosses into the Transition regime

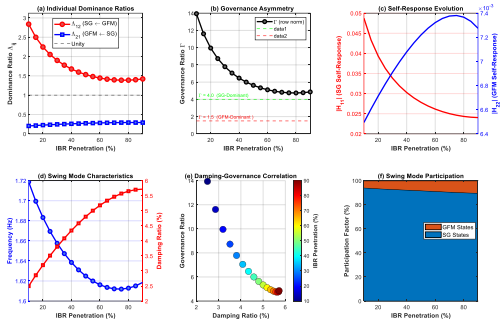


Fig. 7. Governance ratio evolution across IBR penetration range at SCR = 2.

(1.5≤Γ<4). SG dominance is further corroborated by participation factors: 91.2% SG vs. 8.8% GFM at the 60% baseline (Γ=5.11). The erosion of SG frequency authority with IBR penetration is real but bounded; under SCR=2, the SG retains dominant governance across the full studied range.

B. Comparison with the Relative Gain Array (RGA)

To provide a direct, quantitative benchmark against an established multivariable interaction metric, we compare Γ to the RGA [40], computed from the identical 2×2 H-matrix used throughout this study, across the same penetration sweep (SCR = 2).

RGA tracks the same overall trend in interaction strength as Γ across the sweep (correlation r = -0.996 with RGA_{12}). However, RGA is structurally incapable of capturing the directional information central to the proposed framework: for any 2×2 system, RGA(1,2) and RGA(2,1) are algebraically identical, a known structural property of 2×2 RGA [40], since both reduce to the same expression $-H_{12}H_{21}/\det(H)$, which we confirm numerically to machine precision ($max|RGA_{12} - RGA_{21}|$ = 1.11×10⁻¹⁶ across the sweep). Consequently, RGA cannot distinguish 'GFM's influence on SG' from 'SG's influence on GFM,' whereas the proposed $\Lambda_{12}/\Lambda_{21}$ decomposition retains this distinction (Λ_{21} = 0.28 vs. Λ_{12} = 1.44 at baseline, a nearly fivefold asymmetry RGA cannot express in principle).

TABLE III Governance Ratio (Γ) vs. RGA Across IBR Penetration (SCR = 2).

Pen(%)	Γ	RGA_{11}	RGA_{12}	RGA_{21}	RGA_{22}
20	9.956	2.030	-1.030	-1.030	2.030
30	7.787	1.865	-0.865	-0.865	1.865
40	6.467	1.772	-0.772	-0.772	1.772
50	5.630	1.717	-0.717	-0.717	1.717
60	5.11	1.688	-0.688	-0.688	1.688
70	4.825	1.679	-0.679	-0.679	1.679
80	4.742	1.686	-0.686	-0.686	1.686

C. Time-Domain Validation of Governance Directionality

To empirically validate the governance directionality predicted by Γ, nonlinear time-domain simulations were conducted on both the modified IEEE 9-bus and IEEE 14-bus systems. In the 9-bus system, a 0.1 p.u. step disturbance was applied to the input channel of the governed resource. The peak frequency deviation and RoCoF of the governing resource, induced solely through network coupling, were compared with those of the governed resource. As shown in Fig. 8, the governing resource exhibited a 4.8× lower peak frequency deviation and a 7.3× lower RoCoF, demonstrating the SG's immunity to GFM-side disturbances.

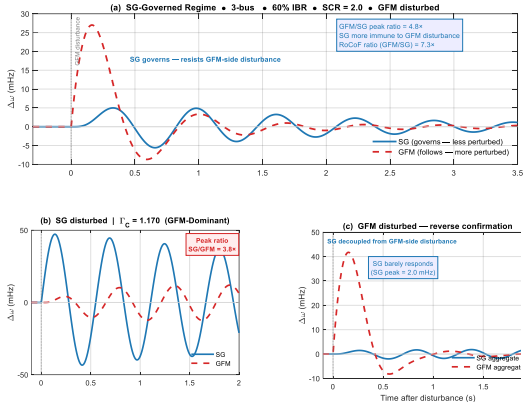


Fig. 8. Time-domain governance directionality validation: (a) 3-bus SG-Dominant (Γ=5.11). (b) 14-bus GFM-Dominant (Γ=1.17). (c) Reverse confirmation.

D. Sensitivity Analysis

To assess the framework's robustness to controller-parameter uncertainty, including parameters not examined in the original submission, we performed two complementary analyses at the baseline operating point: (i) an expanded Monte Carlo robustness study (N=100, ±10% uniform perturbation) across ten parameters, including, newly incorporated in this revision, governor droop (R_{gov}), governor time constant (T_{gov}), AVR gain (K_a), and AVR time constant (T_a) alongside the original H_{SG}, H_{virt}, D_{virt}, ω_{pll}, ω_{cc}, D_p; and (ii) a one-at-a-time (OAT) deterministic sensitivity sweep (±10–30%) of the controller parameters, summarized in a tornado plot (Fig. 9).

TABLE IV Monte Carlo sensitivity summary (N=100, ±10%).

Metric	Mean	Std Dev	CoV%	95% CI	Baseline
f_{swing} (Hz)	1.618	0.054	3.34	[1.541, 1.711]	1.616
ζ (%)	5.169	0.17	3.3	[4.871, 5.508]	5.18
Λ_{12}	1.446	0.062	4.31	[1.334, 1.556]	1.443
Λ_{21}	0.281	0.034	12.18	[0.222, 0.349]	0.283
Γ	5.244	0.845	16.11	[3.791, 7.02]	5.11

Under the expanded ten-parameter perturbation set, the governance classification remains robust: 91% of trials remain SG-Dominant (Γ≥4), 9% fall in the Transition regime, none in the GFM-Dominant regime. GFL participation remains negligible across all samples (mean 0.002%, maximum 0.002%).

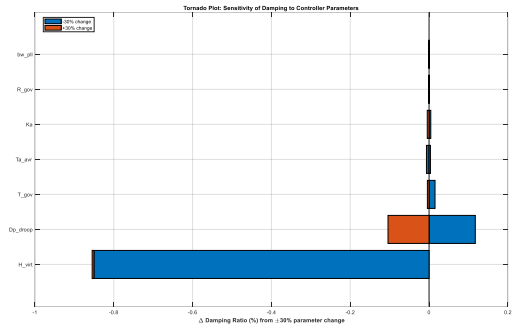


Fig. 9. Tornado plot: sensitivity of swing-mode damping ratio to ±30% variation in each controller parameter.

Virtual inertia (H_{virt}) has by far the largest individual effect on swing-mode damping among the parameters tested. Governor droop, governor time constant, AVR gain, AVR time constant, and PLL bandwidth all exert comparatively negligible influence. This indicates that, unlike in SG-only stability studies where governor and AVR tuning are central design levers, the governance classification in this hybrid system is overwhelmingly shaped by the GFM's virtual-inertia design choice.

IV. VALIDATION OF 2×2 FORMULATION: SG-GFL INTERACTION NEGLIGIBILITY

The H-matrix framework for the modified IEEE 9-bus assumes that GFL inverters have a negligible impact on swing-mode dynamics. This allows for dimensionality reduction from the full 3×3 SG-GFL-GFM model to a more manageable 2×2 SG-GFM formulation. This assumption holds provided that the GFL PLL bandwidth remains well below the swing-mode frequency (in this study, approximately 0.8 Hz PLL bandwidth versus 1.6 Hz swing-mode frequency) and grid strength remains within the moderate-to-strong range studied here (SCR ≥ 1.5). At substantially higher PLL bandwidths, or under very weak grid conditions where PLL dynamics can couple more strongly with electromechanical modes, this simplification should be re-validated rather than assumed. This section validates this assumption through two independent approaches, corroborated by the broadband analysis of Section II-D.

A. SG-GFL Interaction: Modal Analysis

Eigenvector decomposition at the baseline operating point is employed to apportion each resource type's contribution to the swing mode. The resulting participation factors are [17]:

$$p_{SG} = 91.2\%, p_{GFM} = 8.8\%, p_{GFL} = 0.0\% \quad (21)$$

Physical interpretation reveals that this arises from timescale separation [16]: GFL current-control bandwidth ($\omega_{cc} \approx 55\, rad/s$, corresponding to 8 Hz) operates on 20 ms timescales, while electromechanical swing oscillations

exhibit a 625 ms period at 1.6 Hz. During swing-mode transients, GFL power control loops track setpoints sufficiently fast that the inverter appears as a constant power load to slower electromechanical dynamics [32].

B. Time-Domain Validation

Nonlinear time-domain simulation compares the full 40-state system (SG: 6 states, GFL: 16 states, GFM: 18 states) against the reduced 24-state system (SG + GFM only, with GFL eliminated via Kron reduction). Six disturbance scenarios examine response accuracy across diverse operating conditions [41].

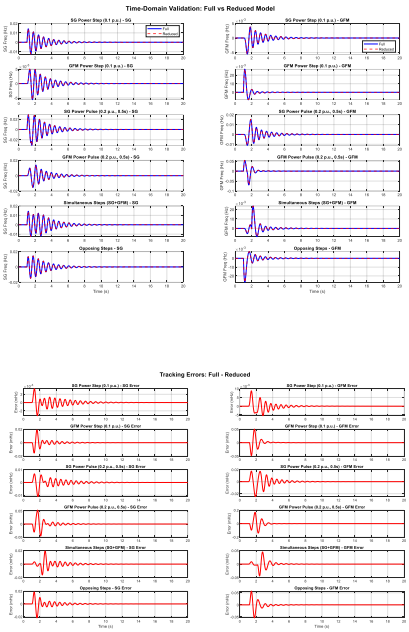


Fig. 10. Full (40-State) vs. Reduced (24-State). a) Time-Domain Validation. b) Tracking Errors.

Tracking accuracy is quantified through root-mean-square error:

$$\varepsilon_{RMS} = \sqrt{\frac{1}{N}\sum_{k=1}^{N}(\omega_{full}(t_k) - \omega_{reduced}(t_k))^2} \qquad (22)$$

computed over 10-second simulation windows with a 1 ms time step. Table V summarizes the results.

TABLE V Time-Domain Validation Results.

Scenario	ωSG Error (μHz)		ωGFM Error (μHz)		Mean
	RMS	Peak	RMS	Peak	(μHz)
SG power step	0.56	3.5	1.4	8.9	0.98
GFM power step	2.4	17.6	6.9	47.5	4.7
SG power pulse	1.6	10.9	4.4	23	3
GFM power pulse	7.6	52	24.1	162.8	15.9
Sim. steps	2.7	18.4	6.4	43.9	4.5

Mean RMS error across all scenarios is 5.7 μHz, representing 0.029% of typical ±20 mHz operational variations [42]. All errors remain negligible relative to practical measurement accuracy and operational frequency variations.

V. DISCUSSION

The H-matrix governance framework outlines key principles for IBR interaction and frequency control in hybrid power systems. This section presents interaction pathways, practical applications, and limitations.

A. Interaction Classification and Pathway Analysis

The proposed framework identifies two distinct IBR interaction pathways in the hybrid SG-GFL-GFM system, each governed by distinct physical mechanisms and operating on timescales that shape swing-mode dynamics.

Dominant SG-GFM inertial interaction: SG and GFM are coupled via inertial dynamics at the swing frequency, and the SG frequency state is 5.11 times more sensitive to GFM disturbances than the GFM is to equivalent SG disturbances. This asymmetry arises from the inertia contrast between the two resource types [27].

Negligible SG-GFL interaction: The interaction between SG and GFL is suppressed by the limited bandwidth of the PLL. Because the GFL synchronization bandwidth (0.8 Hz) is lower than the swing-mode frequency (1.6 Hz), timescale separation establishes a natural interaction barrier [14]. This finding validates the 2×2 formulation from first principles, extending beyond simple participation-factor arguments.

B. Practical Applications

The governance framework suggests several potential operational applications, which we present strictly as motivational directions for future research rather than proven recommendations, as none have been evaluated against real market, grid codes, or field data: (i) coordinated control requirements as a system approaches the Transition regime, where neither resource type clearly dominates and governance-authority erosion accelerates; (ii) interaction-weighted frequency-regulation compensation based on actual participation rather than installed capacity, offering a conceptually motivated alternative to current practices; and (iii) governance-regime trajectory forecasting for long-term reliability planning.

C. Limitations

Several limitations warrant acknowledgment. Single-frequency evaluation overlooks broadband interaction dynamics, and multi-modal systems require frequency-dependent analysis across electromechanical to sub-synchronous ranges [43]. Electromagnetic transients below 1 ms are not considered, and sub-synchronous interaction phenomena require higher-bandwidth models [44].

Although its computational structure allows scaling to larger networks, the framework lacks empirical proof of practical performance on large-scale real-world systems, alternative GFM architectures, varying PLL bandwidths, diverse IBR placement buses, and wider short-circuit-ratio ranges. A preliminary IEEE 14-bus evaluation (Section III-C) confirms that the prediction of governance directionality

extends to a second topology, but comprehensive validation across these dimensions, including sensitivity to resource placement and line contingencies, is still needed before the findings and reported thresholds can be generalized.

Two structural limitations stem from evaluating $H(s)$ at a single real frequency corresponding to the swing mode. First, when multiple electromechanical modes exhibit comparable damping, the selected mode may not fully capture overall system behavior; our broadband analysis (Section II-D) demonstrates this, showing that the GFM self-response term (H_{22}) has a distinct internal resonance near 1.37 Hz, non-coincident with the swing mode. Second, the index Γ relies on absolute values ($|H_{ij}|$), discarding phase information crucial for characterizing oscillatory energy exchange and damping paths among resources. Whether a phase-inclusive or multimodal formulation alters the reported classifications remains an open question.

The present study relies exclusively on numerical simulation; no hardware-in-the-loop or laboratory-scale validation has been performed. The 16-state GFL and 18-state GFM models follow standard control architectures widely used in the literature (e.g., [6], [7], [9], [34], [35]), but their fidelity to real hardware performance has not been independently verified.

VI. CONCLUSION

This paper presents a resource-indexed transfer-function framework for quantifying the interaction authority of IBRs in hybrid power systems incorporating synchronous generators, grid-forming inverters, and grid-following inverters. The H-matrix governance ratio quantifies asymmetric directional interaction through normalized MIMO transfer functions evaluated at the swing-mode eigenvalue, and two pairwise IBR interaction pathways are identified and physically characterized.

An expanded sensitivity analysis, encompassing governor and AVR parameters alongside virtual inertia, damping, and control bandwidths, confirms that the governance classification at the baseline operating point is robust against joint parameter uncertainties up to ±10% and individual parameter variations up to ±30%, with virtual inertia identified as the most influential control parameter tested. We emphasize that the reported thresholds, validation scope, and practical applications discussed herein are illustrative and specific to the systems examined here; Section V-C details the corresponding limitations and outlines specific directions for future work.

This framework enables several practical applications, including interaction-aware grid code requirements, H-matrix-weighted capacity-market compensation, interconnection impact screening using ΔΓ analysis, and reliability planning based on governance-regime trajectory forecasting. Future research directions include multi-modal interaction tracking and PMU-based real-time H-matrix estimation.

REFERENCES

[1] IRENA, “Renewable capacity statistics 2025,” Abu Dhabi, UAE, 2025.
[2] NERC, “2025 long-term reliability assessment,” Atlanta, GA, USA, 2025.
[3] P. (Prabha). Kundur and O. P. Malik, *Power System Stability and Control*, Second. New York, NY, USA: McGraw Hill Education, 2022.
[4] N. Hatziargyriou *et al.*, “Definition and Classification of Power System Stability – Revisited & Extended,” *IEEE Transactions on Power Systems*, vol. 36, no. 4, pp. 3271–3281, 2021, doi: 10.1109/TPWRS.2020.3041774.
[5] J. Matevosyan *et al.*, “A future with inverter-based resources: Finding strength from traditional weakness,” *IEEE Power and Energy Magazine*, vol. 19, no. 6, pp. 18–28, 2021, doi: 10.1109/MPE.2021.3104075.
[6] A. Yazdani and R. Iravani, *Voltage-sourced converters in power systems: modeling, control, and applications*. John Wiley & Sons, 2010. doi: 10.1002/9780470551578.
[7] Q.-C. Zhong and G. Weiss, “Synchronverters: Inverters that mimic synchronous generators,” *IEEE transactions on industrial electronics*, vol. 58, no. 4, pp. 1259–1267, 2010, doi: 10.1109/TIE.2010.2048839.
[8] B. B. Johnson, M. Sinha, N. G. Ainsworth, F. Dörfler, and S. V Dhople, “Synthesizing virtual oscillators to control islanded inverters,” *IEEE Transactions on Power Electronics*, vol. 31, no. 8, pp. 6002–6015, 2015, doi: 10.1109/TPEL.2015.2497217.
[9] J. Rocabert, A. Luna, F. Blaabjerg, and P. Rodriguez, “Control of power converters in AC microgrids,” *IEEE transactions on power electronics*, vol. 27, no. 11, pp. 4734–4749, 2012, doi: 10.1109/TPEL.2012.2199334.
[10] S. Golestan, J. M. Guerrero, and J. C. Vasquez, “Three-phase PLLs: A review of recent advances,” *IEEE Transactions on Power Electronics*, vol. 32, no. 3, pp. 1894–1907, 2016, doi: 10.1109/TPEL.2016.2565642.
[11] J. Huang, K. A. Corzine, and M. Belkhayat, “Small-signal impedance measurement of power-electronics-based AC power systems using line-to-line current injection,” *IEEE Transactions on Power Electronics*, vol. 24, no. 2, pp. 445–455, 2009, doi: 10.1109/TPEL.2008.2007212.
[12] Y. Li, Y. Gu, and T. C. Green, “Revisiting Grid-Forming and Grid-Following Inverters: A Duality Theory,” *IEEE Transactions on Power Systems*, vol. 37, no. 6, pp. 4541–4554, 2022, doi: 10.1109/TPWRS.2022.3151851.
[13] E. A. S. Ducoin, Y. Gu, B. Chaudhuri, and T. C. Green, “Analytical design of contributions of grid-forming and grid-following inverters to frequency stability,” *IEEE Transactions on Power Systems*, vol. 39, no. 5, pp. 6345–6358, 2024, doi: 10.1109/TPWRS.2024.3351530.
[14] J. Z. Zhou, H. Ding, S. Fan, Y. Zhang, and A. M. Gole, “Impact of Short-Circuit Ratio and Phase-Locked-Loop Parameters on the Small-Signal Behavior of a VSC-HVDC Converter,” *IEEE Transactions on Power Delivery*, vol. 29, no. 5, pp. 2287–2296, 2014, doi: 10.1109/TPWRD.2014.2330518.
[15] L. Huang *et al.*, “Grid-synchronization stability analysis and loop shaping for PLL-based power converters with different reactive power control,” *IEEE Transactions on Smart Grid*, vol. 11, no. 1, pp. 501–516, 2019, doi: 10.1109/TSG.2019.2924295.
[16] G. Rogers, *Power system oscillations*, vol. 106. Springer, 2000. doi: 10.1007/978-1-4615-4561-3.
[17] M. J. Gibbard and D. J. Vowles, “Reconciliation of methods of compensation for PSSs in multimachine systems,” *IEEE*

Transactions on power systems, vol. 19, no. 1, pp. 463–472, 2004, doi: 10.1109/TPWRS.2003.820689.
[18] I. J. Pérez-Arriaga, G. C. Verghese, and F. C. Schweppe, "Selective modal analysis with applications to electric power systems, Part I: Heuristic introduction," *ieee transactions on power apparatus and systems*, no. 9, pp. 3117–3125, 1982.
[19] J. Sun, "Impedance-based stability criterion for grid-connected inverters," *IEEE transactions on power electronics*, vol. 26, no. 11, pp. 3075–3078, 2011, doi: 10.1109/TPEL.2011.2136439.
[20] M. Cespedes and J. Sun, "Impedance modeling and analysis of grid-connected voltage-source converters," *IEEE Transactions on Power Electronics*, vol. 29, no. 3, pp. 1254–1261, 2013, doi: 10.1109/TPEL.2013.2262473.
[21] L. Harnefors, M. Bongiorno, and S. Lundberg, "Input-admittance calculation and shaping for controlled voltage-source converters," *IEEE transactions on industrial electronics*, vol. 54, no. 6, pp. 3323–3334, 2007, doi: 10.1109/TIE.2007.904022.
[22]A. Keyhani, *Design of smart power grid renewable energy systems*. John Wiley & Sons, 2016. doi: 10.1002/9781119573265.
[23] B. He, W. Chen, X. Li, L. Shu, Z. Zou, and F. Liu, "Unified frequency-domain small-signal stability analysis for interconnected converter systems," *IEEE Journal of Emerging and Selected Topics in Power Electronics*, vol. 11, no. 1, pp. 532–544, 2022, doi: 10.1109/JESTPE.2022.3201570.
[24] Y. Liao and X. Wang, "Impedance-based stability analysis for interconnected converter systems with open-loop RHP poles," *IEEE Transactions on Power Electronics*, vol. 35, no. 4, pp. 4388–4397, 2019.
[25] R. Eriksson, N. Modig, and K. Elkington, "Synthetic inertia versus fast frequency response: a definition," *IET renewable power generation*, vol. 12, no. 5, pp. 507–514, 2018, doi: 10.1049/iet-rpg.2017.0370.
[26] F. Gonzalez-Longatt, "Impact of synthetic inertia from wind power on the protection/control schemes of future power systems: Simulation study," in *11th IET International Conference on Developments in Power Systems Protection (DPSP 2012)*, IET, 2012, p. 74.
[27] F. Milano, F. Dörfler, G. Hug, D. J. Hill, and G. Verbič, "Foundations and challenges of low-inertia systems," in *2018 power systems computation conference (PSCC)*, IEEE, 2018, pp. 1–25. doi: 10.23919/PSCC.2018.8450880.
[28] P. Tielens and D. Van Hertem, "The relevance of inertia in power systems," *Renewable and sustainable energy reviews*, vol. 55, pp. 999–1009, 2016, doi: 10.1016/j.rser.2015.11.016.
[29] Y. Gu and T. C. Green, "Power system stability with a high penetration of inverter-based resources," *Proceedings of the IEEE*, vol. 111, no. 7, pp. 832–853, 2022, doi: 10.1109/JPROC.2022.3179826.
[30] Z. Wang, Y. Shan, Y. Zhu, R. Liu, and Y. Gu, "Spatio-temporal frequency distribution analysis in systems with grid-forming and grid-following inverters: A new perspective from frequency domain," *IEEE Access*, 2025, doi: 10.1109/ACCESS.2025.3571481.
[31] Z. Rigi and M. Hassanniakheibari, "Enhancing Small-Signal Stability of Multi-Machine Power Systems Using PMU Data," IECO, vol. 9, no. 1, pp. 65-76, Mar. 2026.
[32] P. W. Sauer, M. A. Pai, and J. H. Chow, *Power system dynamics and stability: with synchrophasor measurement and power system toolbox*. John Wiley & Sons, 2017. doi: 10.1002/9781119355755.
[33] M. Liserre, F. Blaabjerg, and S. Hansen, "Design and control of an LCL-filter-based three-phase active rectifier," *IEEE Transactions on industry applications*, vol. 41, no. 5, pp. 1281–1291, 2005, doi: 10.1109/TIA.2005.853373.
[34] S. Buso and P. Mattavelli, *Digital control in power electronics*. Springer Nature, 2022. doi: 10.1007/978-3-031-02499-3.
[35] L. Zhang, L. Harnefors, and H.-P. Nee, "Power-synchronization control of grid-connected voltage-source converters," *IEEE Transactions on Power systems*, vol. 25, no. 2, pp. 809–820, 2009, doi: 10.1109/TPWRS.2009.2032231.
[36] S. D'Arco and J. A. Suul, "Equivalence of virtual synchronous machines and frequency-droops for converter-based microgrids," *IEEE Transactions on Smart Grid*, vol. 5, no. 1, pp. 394–395, 2013.
[37] B. Wen, D. Boroyevich, R. Burgos, P. Mattavelli, and Z. Shen, "Analysis of DQ small-signal impedance of grid-tied inverters," *IEEE Transactions on Power Electronics*, vol. 31, no. 1, pp. 675–687, 2015, doi: 10.1109/TPEL.2015.2398192.
[38] A. NERC and D. GA, "Integrating inverter-based resources into low short circuit strength systems," 2017, *North American Electric Reliability Corporation (NERC) Atlanta, GA, USA*.
[39] W. H. Kruskal and W. A. Wallis, "Use of ranks in one-criterion variance analysis," *Journal of the American statistical Association*, vol. 47, no. 260, pp. 583–621, 1952, doi: 10.2307/2281082.
[40] E. Bristol, "On a new measure of interaction for multivariable process control," *IEEE Trans. Automat. Contr.*, vol. 11, no. 1, pp. 133–134, 1966.
[41] H. K. Khalil and J. W. Grizzle, *Nonlinear systems*, vol. 3. Prentice hall Upper Saddle River, NJ, 2002.
[42] R. S. NERC, "Committee and others. Balancing and frequency control: A technical document prepared by the nerc resources subcommittee," NERC Technical Report; Technical Report; NERC: Atlanta, GA, USA, 2011.
[43] J. Machowski, Z. Lubosny, J. W. Bialek, and J. R. (James R. Bumby, *Power system dynamics : stability and control*, Third. Hoboken, NJ, USA: John Wiley, 2020.
[44] "Terms, Definitions and Symbols for Subsynchronous Oscillations," *IEEE Transactions on Power Apparatus and Systems*, vol. PAS-104, no. 6, pp. 1326–1334, 1985, doi: 10.1109/TPAS.1985.319152.



Shwan Sheikhahmadi was born in Sanandaj, Iran. He received the M.S. degree in electrical engineering from the University of Kurdistan, Sanandaj, Iran, in 2021. He is currently pursuing the Ph.D. degree in electrical engineering at the University of Kurdistan, Sanandaj, Iran. In 2025, he was a visiting Ph.D. student at AAU Energy, Aalborg University, Aalborg, Denmark. His current research interests include power system dynamics and stability, renewable energy integration, and power system modeling and simulation.



Ali Hesami Naghshbandy was born in Sanandaj, Iran. He received his B.S., M.S., and Ph.D. degrees in Electrical Power Engineering from the Iran University of Science & Technology Tehran, Iran, in 1995, 2002, and 2009 respectively. He is currently an Associate Professor at University of Kurdistan, Sanandaj, Iran. His research interests are power system dynamics, stability and control.



Rahmatollah Mirzaei received the B.E. degree in electronic engineering from Tabriz University, Tabriz, Iran, in 1987, the M.Sc. degree in control engineering from Tehran University, Tehran, Iran, in 1991, and the Ph.D. degree in the Power Electronics from Indian Institute of Science in Bangalore, India, in 2007. He is currently an Associate Professor at the University of Kurdistan, Sanandaj, Iran, where he was a Lecturer from 1993. His research interests include design, analysis, control, and modeling of power converters for PFC circuits, soft switching and active filter systems.